CLIMATOLOGY

Constraining the contribution of the Antarctic Ice Sheet to Last Interglacial sea level

Robert L. Barnett[1,2†], Jacqueline Austermann[3*†], Blake Dyer[4], Matt W. Telfer[5], Natasha L. M. Barlow[6], Sarah J. Boulton[5], Andrew S. Carr[7], Roger C. Creel[3]

Polar temperatures during the Last Interglacial [LIG; ~129 to 116 thousand years (ka)] were warmer than today, making this time period an important testing ground to better understand how ice sheets respond to warming. However, it remains debated how much and when the Antarctic and Greenland ice sheets changed during this period. Here, we present a combination of new and existing absolutely dated LIG sea-level observations from Britain, France, and Denmark. Because of glacial isostatic adjustment (GIA), the LIG Greenland ice melt contribution to sea-level change in this region is small, which allows us to constrain Antarctic ice change. We find that the Antarctic contribution to LIG global mean sea level peaked early in the interglacial (before 126 ka), with a maximum contribution of 5.7 m (50th percentile, 3.6 to 8.7 m central 68% probability) before declining. Our results support an asynchronous melt history over the LIG, with an early Antarctic contribution followed by later Greenland Ice Sheet mass loss.

INTRODUCTION

It is extremely likely that global temperatures will be 2°C warmer than preindustrial levels by 2100 (*1*). While predictions of emissions and temperature are somewhat well constrained and depend on Representative Concentration (*2*) or Shared Socioeconomic (*3*) Pathways, the sea-level response to different amounts of warming is less certain (*4*). Furthermore, a greater understanding of the complexities of ice-Earth-ocean processes associated with ice sheets has increased uncertainty in sea-level projections in the AR6 Intergovernmental Panel on Climate Change (IPCC) report (*4*) compared to earlier reports. The current likely range (central 68% probability) of global mean sea-level (GMSL) rise by 2100 from low-end (SSP1-2.6) to high-end (SSP5-8.5) scenarios is 0.33 to 1.02 m (*4*), but this range increases notably when the potential effects of marine ice-cliff instability in Antarctica are considered (*5*, *6*). As mass loss from the Greenland Ice Sheet (GIS) and mountain glaciers closely track temperature, their futures largely depend on emissions scenario (*7*). However, the Antarctic Ice Sheet (AIS) is susceptible to dynamic instabilities from calving, grounding line retreat, basal melting, hydrofracturing, marine ice-sheet instability, and, potentially, marine ice-cliff instability (*8*)—effects that mean that the ice-sheet response to future warming is poorly understood (*9*). This deep uncertainty surrounding nonlinear instabilities of the AIS dominates the uncertainty in sea-level projections (*5*), limiting their usability for managing coastal risk (*10*).

Paleo sea-level data from past warm periods, when GMSL was meters higher than present, can yield crucial insights into how the AIS will respond to warming (*11*). The Last Interglacial (LIG) period is characterized by warmer than present polar temperatures (*12*, *13*) and GMSL 5 to 10 m higher than present day (*4*, *11*). These characteristics are therefore useful for understanding future sea-level rise (*6*, *14*, *15*). However, in general, there remains low agreement in LIG GMSL related to its magnitude [e.g., 6.6 to 9.4 m based on a global data compilation (*16*) to 1.2 to 5.3 m based on data from the Bahamas (*17*)], timing [e.g., sea-level peak early in the LIG in the Seychelles (*18*) versus late in Western Australia (*19*)], structure [e.g., unimodal (*20*), dual-peaked (*16*), or multi-peaked (*21*)], and melt source [GIS or AIS (*4*)]. Currently, constraints for the Antarctic contribution to LIG GMSL have been inferred from relative sea-level (RSL) curves from single regions [e.g., the Seychelles (*6*)] or probabilistic assessments of globally distributed datasets (*16*). To estimate the GMSL contribution from Antarctica, the contributions from all sources (e.g., solid Earth, Greenland, Antarctica, glaciers, and thermal expansion) must be deconvolved from LIG RSL curves, which requires assumptions about each source, particularly the magnitude of GIS mass loss. Most LIG RSL data come from sites in the intermediate and far field of (i.e., distal to) Late Pleistocene ice sheets. However, these locations undergo RSL changes driven by mass loss from both the AIS and GIS (*22*), which makes distinguishing the relative contributions from the different ice sheets challenging (*23*). There is a pressing need for an observationally constrained estimate of the Antarctic contribution to LIG GMSL to better parameterize next-generation GMSL projections, and new data from near-field locations provide this opportunity (*11*, *24*).

Here, we present a new LIG RSL reconstruction for northwest (NW) Europe, a region whose proximity to Greenland makes local sea-level changes not very sensitive to GIS mass loss, particularly in the early LIG (*22*, *24*), but very sensitive to mass loss from Antarctica (Fig. 1, A and B). We report new geochronological controls for three LIG coastal sites in southwest (SW) Britain and compile a database of absolutely dated (i.e., ages are not inferred through relative techniques) LIG coastal features from further 13 sites across NW Europe (Fig. 1; Supplementary Data). Working within a near-field region raises the challenge of large uncertainties in the glacial isostatic adjustment (GIA) correction associated with

[1]Geography, College of Life and Environmental Sciences, University of Exeter, Exeter, UK. [2]Département de biologie, chimie et géographie et Centre d'études nordiques, Université du Québec à Rimouski, Rimouski, QC, Canada. [3]Lamont-Doherty Earth Observatory, Columbia University, Palisades, NY, USA. [4]School of Earth and Ocean Sciences, University of Victoria, Victoria, BC, Canada. [5]School of Geography, Earth and Environmental Sciences, University of Plymouth, Plymouth, UK. [6]School of Earth and Environment, University of Leeds, Leeds, UK. [7]School of Geography, Geology and the Environment, University of Leicester, Leicester, UK.
*Corresponding author. Email: jackya@ldeo.columbia.edu
†These authors contributed equally to this work.

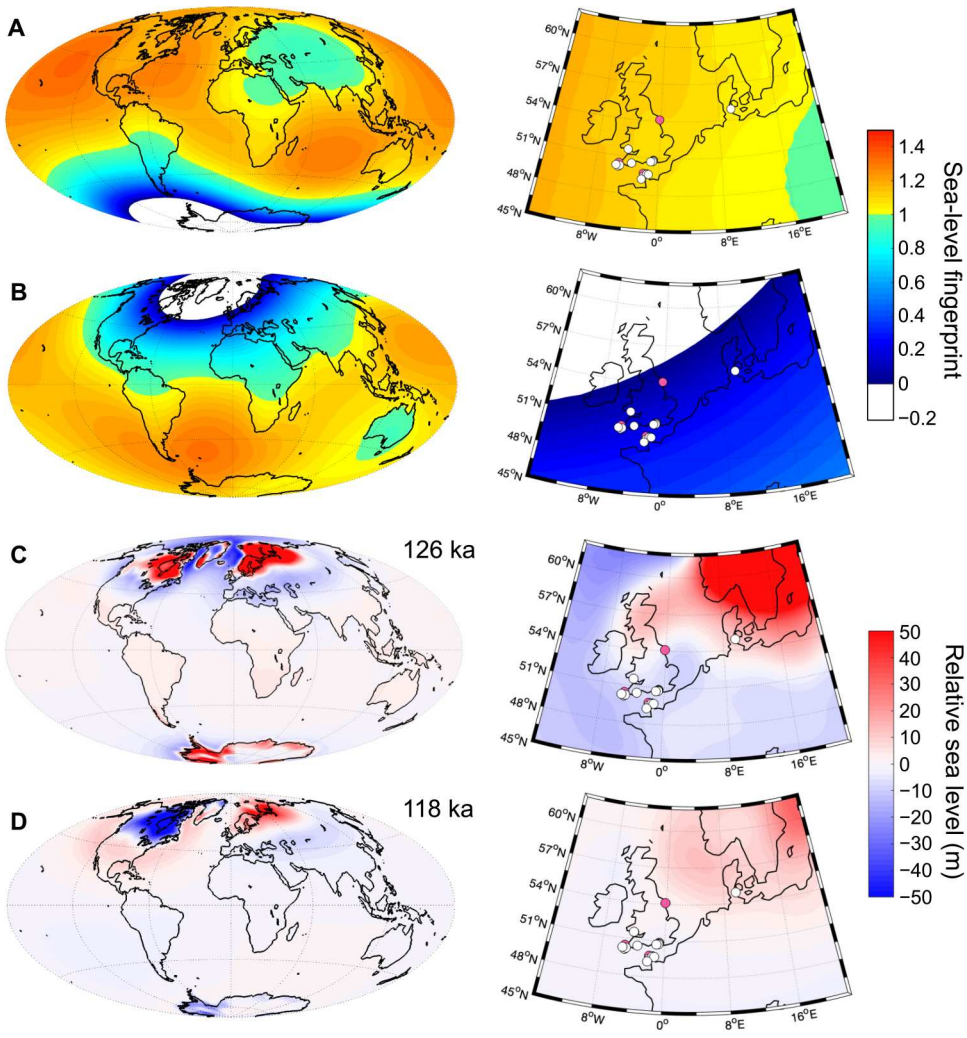

Fig. 1. Sea-level changes from ice-sheet mass loss and gravitational, rotational, and deformational effects. (**A**) Normalized global (left) and regional (NW Europe, right) sea-level changes from instantaneous West AIS (WAIS) mass loss [following Hay *et al.* (*22*)]. The scale is normalized to 1 and demonstrates the sensitivity of NW Europe to WAIS mass loss. White and pink markers denote the location of sea-level index points and sea-level limiting data, respectively. (**B**) Normalized global and regional sea-level changes caused by instantaneous mass loss from the GIS following the ice melt pattern by Calov *et al.* (*38*); white regions are areas of sea-level fall. This demonstrates the general insensitivity of sea level in NW Europe to GIS mass loss. (**C**) Relative sea-level changes due to GIA at 126 ka based on a well-performing GIA model [i.e., 71-km lithosphere thickness, upper and lower mantle viscosities of 0.4×10^{21} and 10×10^{21} Pa s, respectively, an EIS with an ice mass SLE of 40 m, and a slow deglaciation rate; see fig. S1 (G to K)]. (**D**) The same as for (C) but at 118 ka.

Late Pleistocene ice mass changes, here the Eurasian Ice Sheet (EIS) (Fig. 1, C and D) (*25*, *26*). However, our database allows us to reduce the GIA uncertainty by leveraging spatial trends within our data to identify the most likely GIA scenarios within a large range of model runs (n = 600; Materials and Methods). We estimate long-term deformation due to mantle dynamic topography (*27*), crustal deformation, or sediment loading (*28*) using Pliocene marine platforms at each site assuming constant uplift rates. Our data, long-term deformation estimates, and GIA models are combined within a Bayesian framework to infer a regionally self-consistent estimate of the glacial GIA-corrected sea level (see Materials and Methods). We emphasize that "glacial GIA-corrected" refers to GIA corrections related to ice changes before and after, but not during, the LIG. We account for that contribution (interglacial GIA correction) separately by modeling the local sea-level response to a range of GIS melt scenarios during the LIG. The glacial GIA-corrected sea-level estimate, with subtraction of the sea-level contributions from Greenland, mountain glaciers, and thermal expansion, results in a new observationally constrained estimate of the Antarctic contribution to GMSL during the LIG. It is possible that the Laurentide Ice Sheet was still present during the early LIG (*29*), in which case this procedure yields a lower bound for the Antarctic contribution to LIG GMSL.

RESULTS AND DISCUSSION

Coastal sea-level indicators

We present new absolute age constraints for three LIG coastal sequences in SW Britain using optical dating of quartz and K-feldspar sand grains (Materials and Methods). The coastal sequences belong

to the Godrevy Member of the Penwith Formation (*30*) and comprise LIG littoral deposits that occupy (interglacial) wave-cut platforms in Devon and Cornwall (*31*, *32*). Basal intertidal pebble-beach foreshore facies are overlain by sandy beach backshore deposits that, in some locations, grade upward into dune sands. Samples from the basal contacts of the sandy beach backshore deposits at all sites [4.4 to 6.4 m Ordnance Datum Newlyn (ODN)] date to Marine Isotope Stage (MIS) 5e [i.e., 1σ age uncertainties overlap with 129 to 116 thousand years (ka)] (Table 1; Supplementary Data). Two further samples of cemented beach sands unconformably overlying shore platforms with wave-cut notches at elevations of 4.4- and 4.7-m ODN date to late MIS 5e. To estimate local RSL in SW Britain, we correct sample elevations for reference water levels (RWLs) of the associated depositional features and calculate error terms from the indicative ranges of the depositional features (Materials and Methods; Supplementary Data) (*33*). The documented beach facies record the elevation of maximum RSL from which we constrain the mean weighted local LIG RSL highstand in SW Britain to 4.9 ± 1.0 m (1σ).

Our results are compiled into a dataset of LIG RSL features (e.g., marine sediments, beach facies, and dune sands) from across NW Europe (Table 1; Supplementary Data), following established protocols (*33*). We limit the dataset to data derived from absolute-dating approaches comparable to our new age constraints (i.e.,

Table 1. Absolute-dated LIG relative sea-level data from NW Europe including regional weighted means (see also Supplementary Data). RWL, reference water level; IR, indicative range; RSL, relative sea level; T.limiting, terrestrial-limiting data point (i.e., sea level was lower than this elevation)

ID	Location	Feature	Age (ka, ±1σ)	RWL (± IR/2)	RSL (m, ±1σ)
DK1	Jutland	Shoreface-glaciofluvial sands	106 ± 11	2.0 (T.limiting)	16.0 (T.limiting)
DK2	Jutland	Beach deposits	121 ± 13	−0.1 ± 0.24	18.1 ± 0.47
FR1	Normandy	Dune sands	106 ± 10	6.4 (T.limiting)	−1.4 (T.limiting)
FR3	Normandy	Dune sands	107 ± 10	10.5 (T.limiting)	−4.5 (T.limiting)
	Normandy MIS 5d weighted mean (limiting):		**107 ± 7**		**≤−3.0**
FR5	Normandy	Dune sands	111 ± 8	5.9 (T.limiting)	1.4 (T.limiting)
FR7	Normandy	Dune sands	115 ± 12	5.9 (T.limiting)	3.9 (T.limiting)
	Normandy MIS 5e weighted mean (limiting):		**112 ± 7**		**≤2.7**
FR2	Normandy	Beach deposits	115 ± 11	1.4 ± 2.7	4.6 ± 2.7
FR4	Normandy	Beach ridge	118 ± 12	4.1 ± 1.8	3.6 ± 1.9
FR6	Normandy	Beach ridge	121 ± 13	4.1 ± 1.8	5.7 ± 1.9
	Normandy MIS 5e weighted mean:		**118 ± 7**		**4.6 ± 1.2**
FR8	Normandy	Marine sands	126 ± 11	−0.1 ± 2.1	0.4 ± 2.1
UK1	Yorkshire	Dune sands	121 ± 12	11.8 (T.limiting)	−7.8 (T.limiting)
UK2	Sussex	Marine sediments	121 ± 12	0.0 ± 1.7	5.0 ± 1.7
UK3	Sussex	Marine sediments	124 ± 10	0.0 ± 1.6	5.0 ± 1.7
UK4	Sussex	Beach ridge	133 ± 13	4.9 ± 2.7	2.1 ± 2.7
UK5	I. of Wight	Estuarine sediments	115 ± 10	0.0 ± 1.3	6.0 ± 1.3
UK6	Wales	Beach ridge	122 ± 9	7.6 ± 3.7	5.4 ± 3.7
UK7	Wales	Beach ridge	117 ± 23	7.6 ± 3.7	4.8 ± 3.7
	Wales MIS 5e weighted mean:		**121 ± 8**		**5.1 ± 2.6**
UK8	Jersey	Beach deposits	121 ± 14	1.3 ± 2.9	6.7 ± 2.9
UK9	Devon	Marine sediments	116 ± 9	−0.1 ± 1.5	5.8 ± 1.5
UK10*	Cornwall	Beach deposits	120 ± 7	0.3 ± 2.6	4.8 ± 2.7
UK11*	Cornwall	Beach deposits (notch)	119 ± 7	−0.1 ± 2.0	4.8 ± 2.0
UK12*	Cornwall	Beach deposits	115 ± 6	0.4 ± 2.6	4.6 ± 2.6
UK13*	Cornwall	Beach deposits (notch)	115 ± 6	−0.1 ± 2.1	4.5 ± 2.1
UK14*	Cornwall	Beach deposits	141 ± 12	0.3 ± 2.9	6.1 ± 2.9
UK15*	Cornwall	Beach deposits	131 ± 14	0.3 ± 2.9	5.6 ± 2.9
UK16*	Cornwall	Beach deposits	123 ± 12	0.3 ± 2.9	4.5 ± 2.9
	Cornwall MIS 5e weighted mean:		**119 ± 3**		**4.9 ± 1.0**
UK17	Cornwall	Dune sands	116 ± 9	11.3 (T.limiting)	−3.3 (T.limiting)

*New age constraints developed in this study.

luminescence and uranium-series) but recognize that this necessitates an omission of data from age-inferred approaches [e.g., pollen zone associations (*34*)]. The dataset includes MIS 5e beach deposits in NW France (mean weighted age, 118 ± 7 ka, 1σ) that constrain the RSL highstand there to 4.6 ± 1.2 m (1σ). Relatively younger dune sands overlying these beach facies indicate RSL fall and limit the height of RSL to ≤2.7 m during late MIS 5e (112 ± 7 ka, 1σ) and ≤−3.0 m during MIS 5d (107 ± 7 ka, 1σ). The dataset also includes RSL estimates and terrestrial-limiting data points for southern Britain, the Channel Islands, and Denmark (Table 1). Given that the limiting data do not allow us to constrain the height of RSL as their elevation of formation may be significantly above the highest tides, and their potential ages outside the MIS 5e range, we did not include limiting data in the following sea-level modeling.

Glacial GIA-corrected sea level in NW Europe

To correct the LIG sea-level database for GIA, we consider two contributions: (i) GIA driven by ice mass changes before and after the LIG and (ii) GIA driven by ice mass change during the LIG. The first component is assumed to cause most of the spatial variability in sea level in this region (Fig. 1). Using a suite of 600 different glacial GIA models, therefore, allows us to quantify the common sea-level signal in NW Europe after a correction for glacial GIA, which we call "glacial GIA-corrected sea level." In a second step, we consider how much of this regional sea-level signal is driven by Greenland versus Antarctic ice change during the LIG (accounting for both their GMSL and GIA contributions). Our suite of glacial GIA models represents six ice-sheet configurations with varying sea-level equivalent (SLE) ice volumes in the EIS ranging from 23 m [i.e., equivalent to Last Glacial Maximum (LGM) configuration (*35*)] to 70 m (*36*) during the penultimate glacial maximum (PGM) (fig. S1). Each scenario is paired with two penultimate deglaciation rate pathways and uses modern ice extent over the course of the LIG. A glacial GIA prediction is generated by calculating the gravitationally self-consistent sea-level response to ice and water mass load changes on a rotating Earth (*37*) for varying ice-sheet and Earth model parameters (see Materials and Methods).

Beyond GIA effects, the elevation of LIG sea-level indicators can change after deposition due to crustal deformation from tectonics, offshore sediment loading (*28*), and mantle dynamic topography (*27*). We account for the collective effects of this long-term deformation by using the elevation of colocated Pliocene marine platforms (Materials and Methods). We use a Bayesian framework to infer the most likely sea-level curve by calculating the most likely posterior estimates for GIA and long-term deformation given the spatial and temporal distribution of the RSL data, with prior knowledge specified via the range of GIA models and long-term deformation rates described above.

By considering the posterior glacial GIA weights, we are able to infer the more plausible ice-sheet histories and Earth structures identified by the Bayesian inversion. The inversion tends to favor glacial GIA models with EIS geometries containing between 24 and 47 m SLE ice volumes (fig. S2), suggesting that ice volume in Eurasia during the penultimate deglaciation may have been similar to or greater than ice volumes during the LGM. We find that it is unlikely that the EIS contained an SLE of 71 m as suggested by some ice models (*36*). The inversion favors "slow" deglaciation rates (i.e., starting around 140 ka instead of 135 ka; fig. S2) unless paired with a small EIS (i.e., 24-m SLE), in which case relatively faster deglaciation rates are more likely. In terms of Earth structure, the inversion shows no coherent preference for lithosphere thickness or upper mantle viscosity. Trade-offs exist between lower mantle viscosity and ice size; the larger the MIS 6 EIS, the stronger the preference for a smaller lower mantle viscosity (fig. S2).

Our glacial GIA-corrected sea-level estimate shows a high sea level in NW Europe early during the LIG, followed by a gradual sea-level fall after 126 ka (Fig. 2A). The posterior RSL curves for locations in NW Europe (Fig. 2, B to D) differ from the glacial GIA-corrected sea-level estimate because they include the important glacial GIA effect in the region (Fig. 1, C and D). LIG RSL falls in Denmark over the course of the LIG (Fig. 2B) due to crustal rebound. In contrast, RSL peaked late during the LIG in SW Britain (Fig. 2C) and NW France (Fig. 2D) due to GIA subsidence. Note that the large age uncertainties of our RSL data limit our ability

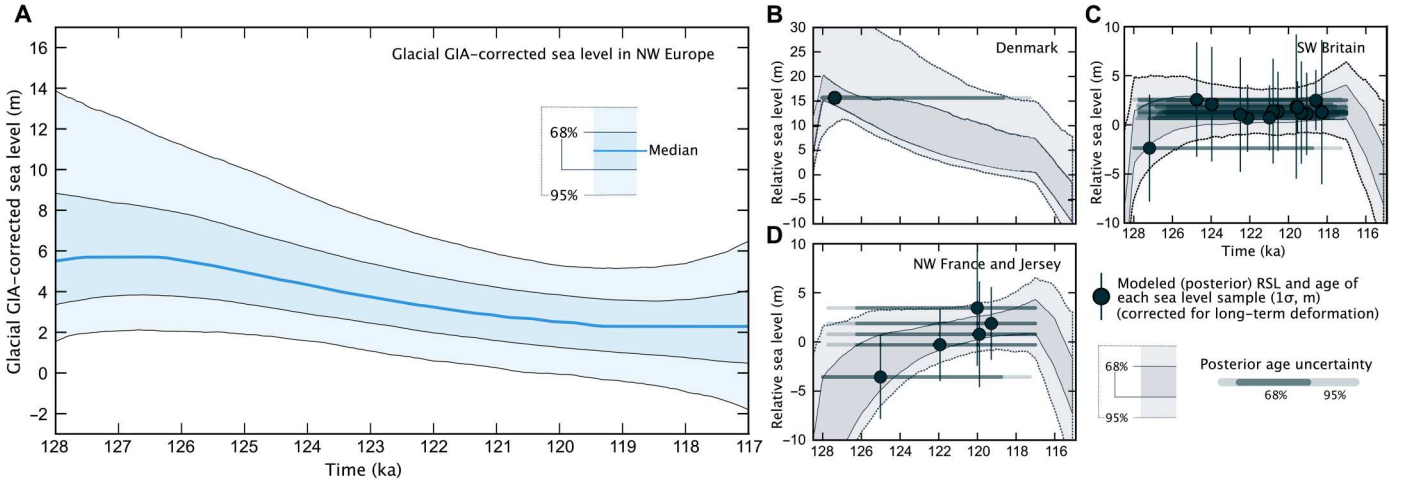

Fig. 2. LIG sea-level highstand in NW Europe. (**A**) Estimated LIG sea level in NW Europe after accounting for long-term deformation and glacial GIA, showing the median (solid blue line) posterior estimate of the Bayesian inversion along with the central 68% (darker shading) and 95% (lighter shading) probabilities. This quantity is only inferred for the time range 128 to 117 ka (see Materials and Methods). (**B** to **D**) Local sea-level model posteriors [shading showing central 68 and 95% probabilities, as in (A)] for specific regions in the database. Note that data elevations have been corrected for long-term uplift, and markers show the most likely posterior age.

to resolve rates of change during MIS 5e. Next, we leverage the low sensitivity of the region to mass loss from Greenland to derive an estimate of the Antarctic contribution to our glacial GIA-corrected sea-level estimate for NW Europe.

Antarctic contribution to LIG GMSL

To estimate the Antarctic contribution to LIG GMSL, we first subtract the effect that Greenland ice change has on sea level in NW Europe. Using Greenland LIG climate ice-sheet models with SLE contributions varying from 0.6 m (*38*) to 5.1 m (*39*) (Fig. 3A and fig. S3), we calculate the regional sea-level expression of these ice histories in NW Europe by accounting for Earth's gravitational, rotational, and deformational response to GIS mass loss. Using the same suite of Earth structures from the Bayesian inversion allows us to produce probability distributions for the Greenland contribution to glacial GIA-corrected sea level in NW Europe (Fig. 3A). As expected from the elastic fingerprint prediction (Fig. 1B), initial mass loss from Greenland leads to only a very small increase in sea level. However, after a few thousand years, viscous deformation starts to counteract the gravitational signal leading to increased local sea-level rise in NW Europe (Fig. 3A and fig. S3). The Greenland sea-level signal in NW Europe significantly lags GIS mass loss, and the magnitude of mean sea-level rise in NW Europe is significantly smaller than the total SLE mass loss from the ice sheet. Taking the mean local sea-level response across all ice and Earth models suggests that the mean Greenland contribution to sea level in NW Europe is likely <1 m and largely occurred during the second half of the interglacial. We note, however, that the magnitude could be up to 3 m at the end of the LIG for an end-member ice history and earth structure combination (see fig. S3). In either case, most of the glacial GIA-corrected sea-level signal early during the LIG (Fig. 2A) is attributable to other processes, most importantly mass loss from Antarctica.

Subtracting the time-varying Greenland contribution from our glacial GIA-corrected sea-level estimate results in a signal that is the combination of the Antarctic and mountain glacier contribution as well as thermal expansion (Fig. 3B) assuming that the Laurentide Ice Sheet had melted by 128 ka. We next correct for contributions from thermal expansion (0.30 ± 0.22 m, 1σ) (*40*) and mountain glaciers (0.32 ± 0.08 m, 1σ) (*41*) assuming that contributions are constant over the LIG. Last, we correct for the GIA effect of AIS mass loss during the LIG to estimate the Antarctic contribution to LIG GMSL. The elastic fingerprint for West and East Antarctic mass loss is close to 1.05 in NW Europe (Fig. 1A) (*22*), but the full GIA effect of LIG AIS change depends on the timing and location of mass loss. Here, we assume a GIA fingerprint effect of LIG AIS change of 1.05 ± 0.05 (1σ) and, as for thermal expansion and mountain glacier contributions, assume a constant value over the LIG. This results in an Antarctic contribution to LIG GMSL that peaked at 5.7 m (50th percentile) (3.6 to 8.7 m; central 68% probability; Fig. 3E). This peak likely occurred at the beginning of the LIG before 126 ka (>68% probability; Fig. 3F) before the Antarctic contribution decreased.

There is remarkable agreement between our estimate of the Antarctic contribution to GMSL during the LIG and the reconstructed SLE ice loss in the Southern Hemisphere from a probabilistic assessment of a globally distributed dataset (Fig. 3C) (*16*); however, we note that our data put a tighter constraint on this quantity. Our study strongly favors early Antarctic ice loss with significant ice regrowth over the course of the LIG, which agrees with some (*42*) but not all (*15*, *43*) AIS models (Fig. 3C). Our central estimate is in excellent agreement with the LIG target range of Antarctic SLE ice loss (3.1 to 6.1 m) used to parameterize sea-level projection models (*6*). This target range is based on an LIG GMSL estimate from the Seychelles of 4.2 to 7.6 m (*18*) paired with the assumption that Greenland had a limited contribution to an early LIG GMSL highstand. We note that our estimate does not require this assumption. A recent reanalysis of Bahamian LIG sea level indicated that GMSL peaked early in the LIG and very unlikely exceeded 5.3 m (*17*). If true, this would require a peak Antarctic contribution on the lower end of our estimated range (i.e., less than 4.4 m if we assume a fingerprint factor of 1.2 for the Bahamas, Fig. 1A, and no early-LIG mass loss from Greenland). However, recent evidence that the Laurentide Ice Sheet may have persisted into the LIG (*29*) would imply that our estimates represent a minimum of the early-LIG Antarctic contribution.

We note that the lower bound of our central estimate of the Antarctic contribution to LIG GMSL (3.6 m; 16th percentile) corresponds closely to potential GMSL rise from collapse of the vulnerable parts of the present-day West AIS (WAIS) (3.2 m) (*44*). In other words, on the basis of our results, there is a less than 12% probability that the WAIS can account for the entire Antarctic contribution to GMSL rise during the LIG. Regardless of whether there was substantial (*45*) or limited (*46*) mass loss from the WAIS during the LIG, our results suggest that additional contributions from other Antarctic sources are likely needed to explain the LIG GMSL highstand (88% probability). While rapid rebound of the bedrock under the WAIS can contribute up to 1 m of GMSL rise from the outflow of meltwater from the continental interior (*47*), this signal is likely smaller during the LIG (*48*). Our results indicate that parts, if not all, of WAIS melted during the LIG or by the end of the penultimate glacial termination, which makes it likely that these sectors will also contribute to sea-level rise in the future.

MATERIALS AND METHODS

NW Europe sea-level database

A database of absolutely dated LIG sea-level indicators from across NW Europe was constructed using new (this study) and published dates (Supplementary Data). To ensure that coastal deposits are associated with the LIG, the database is restricted to dates derived from absolute-dating techniques [in this case, from optically stimulated luminescence (OSL), thermoluminescence, and uranium-series techniques], and only those dates with constrained age uncertainties that overlap with MIS 5e/5d (i.e., 130 to 110 ka) (*49*) are accepted. All dates derive from littoral deposits associated with marine transgression during MIS 5e (e.g., beach sands and gravels, fine-grained estuarine sediments) or marine regression during MIS 5d (e.g., aeolian sands capping littoral deposits). The database comprises 20 sea-level index points (SLIPs) with defined vertical and temporal uncertainties, and 7 terrestrial-limiting (i.e., sea level is known to be lower than a defined elevation) points. References to all original data sources are provided in the Supplementary Data. Where multiple dates from a single facies are given (e.g., as in Jutland, Denmark and Sewerby, UK), a weighted mean and weighted uncertainty is calculated to provide a single chronological control for that facies. The database records environmental

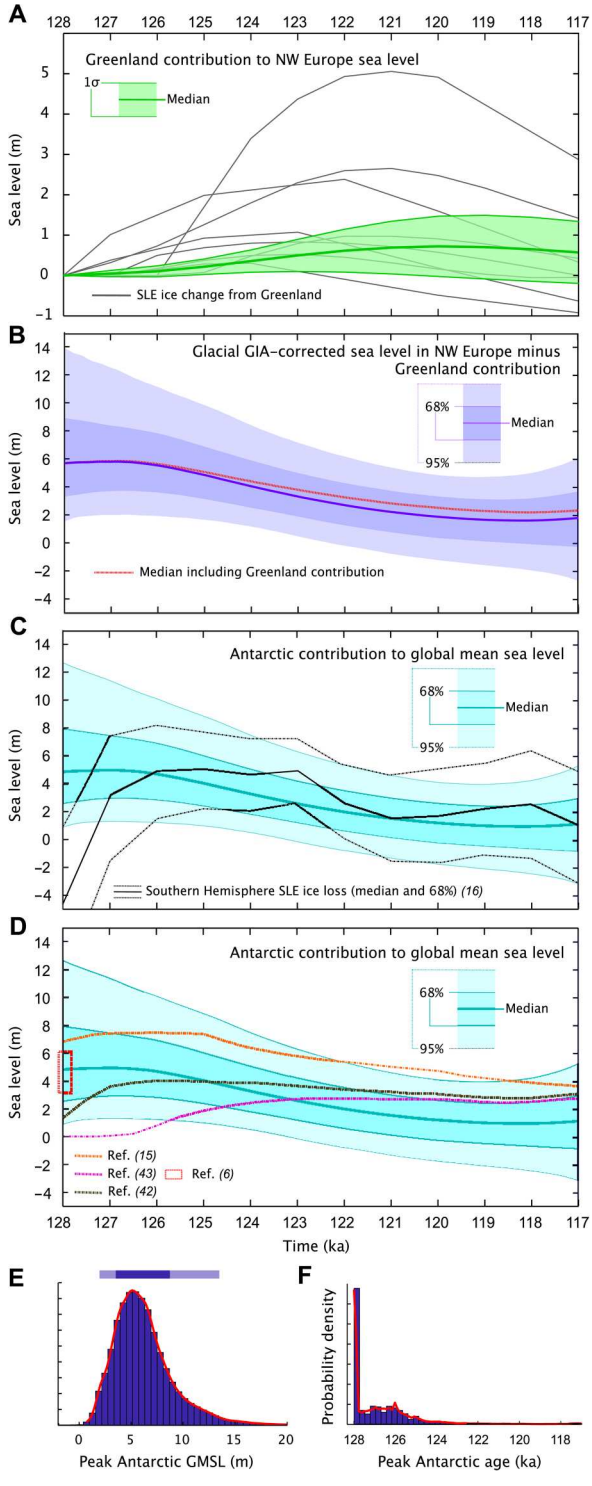

Fig. 3. Greenland and Antarctic contributions to LIG sea level. (**A**) GIS models (n = 8; gray lines) showing global SLE contributions from the ice sheet (gray) and the resulting mean (±1σ) time-varying sea-level change in NW Europe (green line and shading). (**B**) Glacial GIA-corrected LIG sea level in NW Europe, with the Greenland component (A) removed. (**C**) Antarctic contribution to global LIG by removing contributions from glaciers and thermal expansion from (B) and accounting for the GIA signal of Antarctic mass loss. The global Antarctic contribution is compared against SLE ice loss from the Southern Hemisphere (*16*) in (C) and compared against SLE mass loss from Antarctica (*15*, *42*, *43*) and the target range of LIG Antarctic SLE mass loss used to parametrize projection models (*6*) in (**D**). (**E** and **F**) Probability density functions of the magnitude (E) and timing (F) of peak Antarctic contributions to GMSL during the LIG. The bar above (E) demonstrates the central 68% (darker) and 95% (lighter) probability.

depositional interpretations of dated facies to support the calculation of RWLs and indicative ranges. Dates from Jutland, Denmark derive from intertidal beach deposits and overlying shoreface-glaciofluvial sands. Dates from five sites across Normandy in France derive from intertidal beach and beach ridge deposits and overlying aeolian dune sands. Published dates from the United Kingdom represent intertidal beach, beach ridge, marine and estuarine sediments, and aeolian dune sands from sites in South Wales, Yorkshire, Sussex Devon, Cornwall, the Isle of Wight, and Jersey. We do not recalculate ages with updated decay constants; however, updates would be small compared to the age uncertainty. The database includes documented elevations of the basal and upper contacts for each dated facies. A uniform 0.4-m uncertainty is assigned to

each contact elevation to account for variability across survey techniques and for the spatially variable height of the contacts (*33*).

Dating results

A detailed description of the luminescence analytical methods is provided in the Supplementary Materials.

Quartz

The Godrevy and Bream Cove samples generally produced rapidly decaying OSL signals (fig. S4) and exhibited low levels of signal recuperation, reproducible growth curves (low numbers of recycling ratio rejections for both high and low dose recycling points), and satisfactory dose recovery (table S1). Both the Godrevy and Bream Cove samples showed little sensitivity to the choice of preheating temperature (fig. S5). Together, these observations imply suitability of the single-aliquot regenerative-dose (SAR) protocol for quartz. In contrast, the Pendower samples, particularly PEN13-2, were characterized by low OSL sensitivities (fig. S4), and despite the use of early background signal subtraction, up to 25% of aliquots exhibited unacceptable levels of signal recuperation, as well as high recycling ratio rejection rates.

Three Godrevy samples produced quartz OSL ages within uncertainties of one another (table S2), and all ages fall within the range of MIS 5e. Both the Godrevy and Bream Cove samples exhibited equivalent doses in excess of 150 Gy, although the samples exhibit growth in sensitivity-corrected OSL beyond 390 Gy (fig. S4). Nonetheless, these equivalent doses are relatively high compared to the expected saturation point of the quartz fast component and fall within a De range for which age underestimation has in some instances been reported [e.g., (*50*)], albeit not in all cases [e.g., (*51*, *52*)].

We evaluated the proximity to saturation further by considering the dose-response curves obtained when fitting a single saturating exponential fit of the form: $I = I0(1 - \exp[-D/D0])$, where I is the luminescence intensity, $I0$ is the saturation intensity, D is the dose (Gy), and $D0$ (Gy) is the "characteristic dose." The characteristic dose parameter D0 provides a measure of the degree of saturation whereby $2 \times D0$ is equal to ~87% of saturation and is often considered a prudent measure of an aliquot's proximity to saturation [e.g., (*53*)]. For most aliquots, the saturating exponential fit provided an adequate characterization of the dose response, and equivalent doses with finite uncertainties could be estimated. Central Age Model (CAM) equivalent doses also did not differ significantly from those obtained when using a saturating exponential plus linear fit, except for GOD-4 (in this instance, 207 ± 11 Gy 243 ± 13 Gy). The ratio of De to D0 for the three Godrevy samples (dosed to 404 Gy) was 2.2 ± 0.6, 2.5 ± 0.5, and 2.1 ± 0.7 (mean ratio and SD for GOD-2, GOD-3, and GOD-4 respectively). For 3 of the 17 measured GOD-3 aliquots, it was not possible to interpolate an equivalent dose and/or finite equivalent dose uncertainty using a single saturating exponential fit. For Bream Cove (BRM), the De/D0 ratios are lower (2.0 ± 0.7 and 1.6 ± 0.9) but still quite close to the 2D0 threshold.

These data suggest that the samples are potentially close to the limits of the quartz SAR method. However, as shown below, for BRM, the quartz ages are entirely consistent with the K-feldspar results, implying that a De/D0 ratio of ~1.5 to 2.0 does not necessarily preclude a reliable quartz age estimate. Unfortunately, the Godrevy K-feldspar fractions were not available for analysis, precluding a comparable check. However, given the sample context, pending further analysis, we consider the present Godrevy quartz ages to be parsimonious.

Inter-aliquot scatter was low [overdispersion, sensu (*54*) of 11 to 19%] (figs. S6 and S7). For both Bream Cove and especially Pendower, however, calculated equivalent doses from quartz resulted in more widely dispersed age estimates, with higher overdispersion (i.e., inter-aliquot scatter) of 20 to 27%. In the case of Pendower, the quartz OSL ages were also stratigraphically inverted.

Infra-red stimulated luminescence (IRSL) dating

pIRIR estimates were obtained for the Pendower and Bream Cove K-feldspar fractions (<2.58 g cm^{-3}). K-feldspar yields were very low, which limited the number of analyses that could be undertaken. Unfortunately, the Godrevy K-feldspar fractions were lost in initial quartz preparations. In all samples, the residual IRSL signal was tested following 48 hours of daylight exposure, while the suitability of the pIRIR SAR protocol was also assessed via several dose recovery experiments. For Bream Cove, although the $pIRIR_{225}$ (*55*) protocol produced negligible fading rates (g value ~1% per decade), the residual ("unbleachable") signal remaining after 2 days of daylight exposure was ~20 Gy (table S1), which amounts to 8 to 9% of the sample equivalent dose. The residual doses increased substantially with the $pIRIR_{290}$ method. Dose recovery results for the $pIRIR_{225}$ method were acceptable given the measurement uncertainties (table S1). A lower temperature (170°C) second infrared stimulation and a commensurately lower preheating temperature [i.e., 200°C; (*56*)] reduced the residual signal (to 12 to 17 Gy or 5 to 6% of the sample D_e; table S1). The fading rate also remained relatively low (g value <1.5% per decade; see below). We therefore derived all K-feldspar equivalent doses using the $pIRIR_{170}$ protocol, with no measured residual subtracted from the final equivalent dose estimate. The K-feldspar equivalent doses for the Bream Cove and Pendower samples are shown in table S2. In all cases, growth in the sensitivity-corrected IRSL signal continued beyond 400 Gy (fig. S8), and the equivalent dose distributions showed low overdispersion (0 to 8%; fig. S9). Fading rates [following (*57*)] determined following administration of a 35-Gy beta dose and with measurement delays ranging from 0.1 to 185 hours were 3 to 4% per decade for the 50°C IRSL signal and below 1.5% per decade for the $pIRIR_{170}$ signal. Following (*58*), the latter is considered negligible and no fading corrections were applied. The resulting $pIRIR_{170}$ ages for Bream Cove and Pendower are stratigraphically consistent, and less scattered than the quartz estimates, both in the sense of the reduced inter-aliquot scatter resulting in greater precision and in terms of intersample consistency. Hence, these ages are used as the most likely indicators of site age in all subsequent analyses.

Calculating past local sea level from observations

Indicative ranges for the littoral facies were developed by correlating inferred depositional environments with modern-equivalent formational limits. Global tidal and wave models (*59*) were used to compute the modern upper and lower formational limits of beach deposits (ordinary berm to breaking depth), estuarine and marine sediments, and tidal notches (mean higher high water to mean lower low water). The global tidal and wave models were incapable of accurately computing the elevation of storm wave swash height (SWSH) associated with formational limits of beach ridge (upper formation limit) and foredune (lower formation limit) features (*59*). Instead, SWSH (defined as the maximum elevation reached by waves during storm events) was estimated from the elevation

of unvegetated beach ridge crests associated with active modern systems at each site using Google Earth Pro (v. 7.3.3.7786). A similar approach was used to estimate upper formation limits for dune sands by identifying the maximal elevation of vegetated foredune crests. At all relevant sites, vegetated foredune crests tended to occur c. 10 m above the elevation of active unvegetated beach ridge crests (i.e., 10 m above SWSH). The upper limit of modern dune sand formation was therefore assigned SWSH +10 m, which provided a conservative upper limit for a one-tailed uncertainty distribution associated with terrestrial-limiting LIG dune sand deposits.

The position of former RSL is a function of the elevation of the deposit and the RWL associated with the deposit (*33*, *60*). The RWL for each deposit is taken to be the midpoint of the upper and lower modern formational limit of the deposit (*33*), with the exception of limiting index points where the RWL is equal to the lower (marine limiting) or upper (terrestrial limiting) modern formational limits of the deposit. For SLIPs, RSL is then equal to the difference of the elevation of the sample (or deposit) and the RWL of the deposit. The range in formational elevation of the modern deposit (i.e., the indicative range) is taken to represent the 2σ vertical uncertainty associated with the sample (or deposit). Here, the elevation for precise SLIPs is taken to be the upper contact of the littoral facies used to determine the indicative range, whereas for terrestrial-limiting index points (e.g., dune sands), the elevation is taken as the basal contact of the deposit. Uncertainties for SLIPs are root mean square errors of the indicative ranges and a ubiquitous 0.40-m survey error (*33*) to account for measurement and rounding errors and variability in the elevation of deposit contacts. Uncertainties associated with precise SLIPs are assumed to have Gaussian distributions in both time (*x* axis) and space (*y* axis). Changes in the coastline and climate during the LIG (compared to modern) can potentially amplify the tidal range (*61*) or reduce the storm surge height (*62*). This uncertainty is acknowledged here, but not added to our data since it is difficult to quantify the appropriate uncertainty that this introduces at our specific locations.

Long-term deformation

Independent of the effects of GIA associated with Late Pleistocene (de)glaciations, the elevation of sea-level indicators such as littoral deposits can alter after deposition due to tectonic crustal deformation, sediment loading (*28*), and mantle dynamic topography (*27*). At a passive margin, like our sites, rates associated with these processes are relatively small and constant over the Plio-Pleistocene, but can still add up to several meters since the LIG and therefore deformation associated with these processes needs to be accounted for. To correct for these collective effects (which we will refer to as "long-term deformation"), we use site-specific indicators of vertical land motion from outside of the Pleistocene. Most of our long-term deformation indicators are Pliocene marine rock platforms that are colocated with 24 of the 27 data points in our database (see the Supplementary Materials and Supplementary Data for details).

To estimate an uplift rate based on Pliocene platform elevations, we first calculate how much GIA affects their elevation and do so following the procedure described by Dumitru *et al.* (*63*) assuming an age range of 3 to 5 million years (Ma) (Supplementary Data). Note that in contrast to Dumitru *et al.* (*63*), we do not use different GMSL histories but instead use the one that best matches their GMSL estimates, which is based on scaling the LR04 oxygen isotope stack (*64*). Once corrected for GIA, long-term deformation (in all cases—uplift) is calculated for each data point using the GIA-corrected elevation, the age of the Pliocene marine rock platforms (3 to 5 Ma, uniform distribution), and estimate of GMSL [19 ± 8 m, 1σ, (*63*); see Supplementary Data]. GMSL was likely highest during the Early Pliocene and therefore best explains the extensive flat marine rock platforms found across parts of Europe. The GMSL distribution is in line with the Pliocene sea-level highstands by Miller *et al.* (*65*), which average around 16 ± 14 m (1σ). A distribution of uplift rate R at each location is then calculated from the elevation E through

$$R = (E - \mathrm{GIA} - \mathrm{GMSL})/\mathrm{age}$$

where we sample each individual distribution to propagate uncertainties. The resulting distributions are mostly normal with a slight skew toward lower values. Mean values range from 3.5 to 4.5 m of uplift since 125 ka with 1σ uncertainties of around 0.7 m. We report the mean and 1σ values for each site in the Supplementary Data and use them in the following inference.

No Plio-Pleistocene platforms or deposits are available as counterparts to the data points from Denmark, largely due to Late Cenozoic uplift and erosion of the eastern North Sea Basin [e.g. (*66*)]. Late Miocene shallow marine sands that form part of the Oligocene-Miocene sedimentary sequence stratigraphy of Denmark (*67*) and the wider North Sea region (*68*) outcrop at the western edge of Denmark at the Marbaek Klint exposure and form part of the upper Miocene Gram Formation (*67*). These are the youngest deposits that might provide a long-term signal of vertical land motion in Danish onshore stratigraphy. The shallow marine sands of the Marbaek Formation in western Denmark represent a high-energy, tidally influenced shoreface environment (*67*). This formation represents a shallow sea that extended into central Denmark c. 100 m above present-day sea level up until the Late Miocene (*67*, *69*). We are therefore able to estimate a priori long-term uplift rates for data points from Denmark using an elevation of 100 ± 10 m (we conservatively double the uncertainty estimate for this long-term deformation indicator). As for the Pliocene platforms, we correct for GIA assuming a Late Miocene age range of 5 to 7.5 Ma. We estimate that GMSL was 4 ± 17 m (1σ), which is based on the distribution of GMSL highstands during this time period by Miller *et al.* (*65*). Note that GMSL estimates during the Late Miocene by Miller *et al.* (*65*) are lower than Pliocene GMSL estimates. The same procedure as described above yields an estimate of uplift since the LIG at this location of 2.43 ± 0.53 m (1σ).

Geologic markers of long-term deformation are absent in York. Since limiting data are not used in our inversion, we have not attempted to estimate an uplift correction for this data point.

GIA modeling

We use the gravitationally self-consistent sea-level theory described in (*37*) to calculate the response of the solid Earth's gravity field, to changes in ice and ocean load. This calculation allows for shoreline migration and includes feedbacks on Earth's rotation axis. In our GIA calculations, we assume that the Earth's elastic structure follows the preliminary reference Earth model (*70*) and vary three parameters of the viscous structure: a lithospheric thickness that is either 71 or 96 km, an upper mantle viscosity that ranges from 0.3×10^{21} to 0.5×10^{21} Pa s, and a lower mantle viscosity that ranges from 3×10^{21} to 40×10^{21} Pa s. Combining these values leads to 48

different models of Earth's viscosity. In addition to the Earth structure, we prescribe the past ice-sheet history. We will first describe the ice histories over the glacial cycles used to obtain the glacial GIA-corrected sea-level estimates and then the ice history of Greenland mass loss used to infer the Antarctic sea-level contribution during the LIG.

For the deglaciation, we follow the ice history ICE-6G (*35*). Before the LGM, we use the GMSL estimate by Waelbroeck *et al.* (*71*) back to 400 ka and at each time assign the ice geometry from the deglaciation that corresponds to the same GMSL value. The GMSL during the LIG is set to zero, and the GMSL curve before the LIG is shifted back by 3.5 ka to result in a PGM age of 135 ka. This ice history from 400 ka to present forms the basis of our GIA calculation. While the ice history over the last deglaciation is relatively well known, there is ample evidence that the ice-sheet configuration during the PGM (and penultimate deglaciation) was significantly different, in both the distribution of ice (*25*, *36*) and timing of ice loss (*43*). We therefore produce 12 ice models that pair six different ice geometries with two different ice loss timings. For the EIS during the PGM, we start with three published ice geometries: ICE-6G (our base model), Lambeck *et al.* (*25*), and Colleoni *et al.* (*36*). Note that the latter two argue for a much larger EIS, which is supported by more extensive terminal moraines during MIS 6 (*72*). While the SLE ice volume of the EIS during the LGM is only 23.4 m in ICE-6G, the volume increases to 54 and 70 m in the models for the PGM by Lambeck *et al.* (*25*) and Colleoni *et al.* (*36*), respectively (see fig. S1, A, E, and F). This increase in ice volume affects LIG sea level around the globe (*73*, *74*). While the GMSL history before the PGM is also uncertain (*75*), its effect on GIA is small compared to uncertainties related to the ice-sheet size and distribution (*73*). To construct a full penultimate glacial cycle, we first use our base ice model and isolate the EIS contribution to GMSL. Since this ice history is based on ICE-6G, the contribution is around 23.4 m during the PGM. Next, we scale this GMSL contribution of the EIS up to match the ice volume of the Lambeck *et al.* (*25*) and Colleoni *et al.* (*36*) ice volume. We then use the deglacial GLAC-1D ice history by Tarasov *et al.* (*76*) as our template for EIS collapse. We assume that the last 10 m of EIS contribution comes from this ice model. Beyond a GMSL contribution of 10 m, we use a combination of the GLAC-1D ice history (unscaled but fluctuating in accord with the EIS contribution to GMSL) and a scaled version of the selected PGM EIS. The scaling is chosen to obtain a desired EIS contribution to GMSL. The two contributions are combined by taking the maximum ice height between the two at each location. In addition to the three PGM ice configurations mentioned above, we construct three additional PGM models that are versions of the Lambeck *et al.* (*25*) ice model that is reduced in size (by scaling its height) to obtain a PGM SLE value for the EIS of 32, 40, and 47 m (see models LG_32, LG_40, and LG_47 in fig. S1, B to D). The rest of the glacial cycle is constructed as described above.

In all of these scenarios, we balance a larger EIS by reducing the size of the Laurentide Ice Sheet. In addition to the GMSL history by Waelbroeck *et al.* (*71*), we use a slightly modified version during the penultimate glacial cycle with a slower penultimate deglaciation. This earlier onset of the deglaciation is based on a Tahitian coral record (see fig. S1l) (*77*). The six ice geometries paired with two GMSL scenarios yield 12 different ice histories that are paired with the 48 viscosity structures to produce 576 different GIA models. We further pair the ICE-6G–based ice history with a range of Earth structures that have a thinner lithosphere (48 km) for an additional 24 GIA simulations. Combined, this produces 600 GIA runs that are used in this study.

This way of constructing the ice sheet leads to a collapse history that we deem relatively realistic in Fennoscandia given that this part of the ice sheet was a major contributor during the penultimate deglaciation. However, the ice sheet is likely too flat toward its southeastern edge in many of the models given the simplistic scaling (see fig. S1, G to K). The detailed ice geometry in that region is likely to be less crucial for our data that are located in NW Europe. In the absence of a range of existing ice-sheet models for the penultimate deglaciation, we consider that our reconstructions still represent a useful suite of ice histories to test the sensitivity of our glacial GIA models to this input.

To model the GIA signal associated with melting of the GIS over the course of the LIG, we use the same computational model and range of viscosity structures as described above. For the ice history, we use eight published GIS models for the LIG: the high and low scenario by Calov *et al.* (*38*), the Institut Pierre-Simon Laplace (IPSL) anomaly experiment by Quiquet *et al.* (*78*), the most likely scenario by Yau *et al.* (*39*), the three scenarios by Goelzer *et al.* (*79*), and a model based on Bradley *et al.* (*80*). In each case, we linearly interpolate the ice history to 1-ka time steps over the course of the LIG and only start reducing the ice sheet once the ice volume decreases below present values. The local sea-level response in NW Europe is relatively uniform across the region (see Fig. 1A and fig. S3). Small differences from one place to the next can still exist, and those are propagated into the local sea-level uncertainty. For each ice model, we calculate local sea level by taking the mean and SD across the GIA predictions for each location and each viscosity structure. The resulting local sea-level prediction for each Greenland ice history is shown in fig. S3. For the combined local sea-level prediction (Fig. 3), we take the mean and SD at each time step from all data locations, viscosity structures, and ice histories.

Bayesian inversion to infer glacial GIA-corrected sea level

We model LIG glacial GIA-corrected sea level in northern Europe as a Gaussian process, and we fit this Gaussian process to glacial GIA-corrected sea-level data. The mean and covariance components of the Gaussian process are inferred from the paleo-RSL data corrected for each of the 600 potential glacial GIA models using Bayesian inversion. In the inversion model, paleo-RSL data and the associated uncertainty in sample age, elevation, and indicative meaning are treated explicitly as random variables (prior distributions). We estimate the relative probability that each of the 600 glacial GIA models can explain the observations using Bayesian model averaging. Bayesian model averaging provides weights for each of the 600 glacial GIA models, and these weights are used to create a meta-model that combines information learned from each model-data comparison. The next section will describe the details of the inversion model and motivation for those choices.

We remove glacial GIA and long-term uplift from each sea-level observation with the following equation (referred to as GIA-corrected sea level)

$$\text{glacial GIA-corrected sea level} = \text{RSL} - \text{UPLIFT} - \text{GIA}$$

For each index point, RSL is set to a Gaussian distribution with μ = RSL and σ = RSL error.

The uplift and glacial GIA corrections for each observation depend on the age and location of the sample. The ages are treated as Gaussian distributions with μ and σ set to the mean and SD determined from the absolute geochronologies (Supplementary Data). In addition, the age distributions are bound to the LIG (as defined in our glacial GIA model simulations; 128 to 117 ka). For each sample of the posterior, ages are drawn from this distribution, and then the location-specific glacial GIA correction, using a single glacial GIA model, for that age is applied to the sample. In addition, an uplift correction is applied to the observation using the posterior age sample and the regional uplift rate.

We then fit a Gaussian process to the set of glacial GIA-corrected sea-level data. The covariance kernel of the Gaussian process is assumed to be the sum of a radial basis function and a white noise kernel. The radial basis function has two parameters that are learned during the inversion: the variance, σ^2, and the length scale, l. The prior distribution for the length scale is modeled as an inverse Gaussian distribution with μ = 2 and λ = 5. This length scale effectively ignores changes on short time scales (hundreds of years) and time scales longer than the LIG (>10 ka). A normal Gaussian distribution with μ = 0 and σ = 5 is used as a prior for the square root of the variance of the RBF function. A half (positive only) Student-t distribution with ν = and σ = 0.1 is used as a prior for the variance of the white noise kernel. The prior distribution for the mean of the Gaussian process is modeled as a normal Gaussian distribution centered at 0 with an SD of 10.

We sample the posterior distributions with a No U-Turn Sampler (NUTS) using the Python probabilistic programming package PyMC3. The posterior distribution for GIA-corrected sea level was calculated for each glacial GIA model separately. We use leave-one-out cross-validation (LOO) to determine relative probabilities, or weights, that describe the predictive power of each glacial GIA model (in other words, these weights show how well the model performs at predicting observations that are withheld from model training). For example, a glacial GIA model that completely removes all spatial variations in the paleo sea-level data should have a relative probability of 1 when compared to a suite of other, less well-fitting models. The weights are then used to create a weighted mean for glacial GIA-corrected sea level that incorporates all 600 glacial GIA models. One realization of the posterior in this weighted-mean meta-model is generated by combining individual posterior realizations from each of the 600 glacial GIA models, sampled at the relative weight of each model. Generally speaking, we continue to generate new realizations of this posterior until the statistics of interest stop changing significantly. In other words, when the posterior mean and variance start to converge, enough realizations have been generated.

Supplementary Materials

This PDF file includes:

Supplementary Text
Figs. S1 to S9
Tables S1 and S2
Legend for Supplementary Data
References

Other Supplementary Material for this manuscript includes the following:

Supplementary Data

REFERENCES AND NOTES

1. A. E. Raftery, A. Zimmer, D. M. W. Frierson, R. Startz, P. Liu, Less than 2°C warming by 2100 unlikely. *Nat. Clim. Change* **7**, 637–641 (2017).
2. D. P. van Vuuren, J. Edmonds, M. Kainuma, K. Riahi, A. Thomson, K. Hibbard, G. C. Hurtt, T. Kram, V. Krey, J.-F. Lamarque, T. Masui, M. Meinshausen, N. Nakicenovic, S. J. Smith, S. K. Rose, The representative concentration pathways: An overview. *Clim. Change* **109**, 5–31 (2011).
3. K. Riahi, D. P. van Vuuren, E. Kriegler, J. Edmonds, B. C. O'Neill, S. Fujimori, N. Bauer, K. Calvin, R. Dellink, O. Fricko, W. Lutz, A. Popp, J. C. Cuaresma, K. C. Samir, M. Leimbach, L. W. Jiang, T. Kram, S. Rao, J. Emmerling, K. Ebi, T. Hasegawa, P. Havlik, F. Humpenoder, L. A. da Silva, S. Smith, E. Stehfest, V. Bosetti, J. Eom, D. Gernaat, T. Masui, J. Rogelj, J. Strefler, L. Drouet, V. Krey, G. Luderer, M. Harmsen, K. Takahashi, L. Baumstark, J. C. Doelman, M. Kainuma, Z. Klimont, G. Marangoni, H. Lotze-Campen, M. Obersteiner, A. Tabeau, M. Tavoni, The shared socioeconomic pathways and their energy, land use, and greenhouse gas emissions implications: An overview. *Glob. Environ. Change* **42**, 153–168 (2017).
4. B. Fox-Kemper, H.T. Hewitt, C. Xiao, G. Aðalgeirsdóttir, S.S. Drijfhout, T. L. Edwards, N.R. Golledge, M. Hemer, R.E. Kopp, G. Krinner, A. Mix, D. Notz, S. Nowicki, I.S. Nurhati, L. Ruiz, J.-B. Sallée, A.B.A. Slangen, Y. Yu, Ocean, cryosphere and sea level change, in *Climate Change 2021: The Physical Science Basis. Contribution of Working Group I to the Sixth Assessment Report of the Intergovernmental Panel on Climate Change*, V. Masson-Delmotte, P. Zhai, A. Pirani, S.L. Connors, C. Péan, S. Berger, N. Caud, Y. Chen, L. Goldfarb, M.I. Gomis, M. Huang, K. Leitzell, E. Lonnoy, J.B.R. Matthews, T.K. Maycock, T. Waterfield, O. Yelekçi, R. Yu, B. Zhou, Eds. (Cambridge Univ. Press, 2021), pp. 1211–1362.
5. R. E. Kopp, R. M. DeConto, D. A. Bader, C. C. Hay, R. M. Horton, S. Kulp, M. Oppenheimer, D. Pollard, B. H. Strauss, Evolving understanding of antarctic ice-sheet physics and ambiguity in probabilistic sea-level projections. *Earth's Future* **5**, 1217–1233 (2017).
6. R. M. DeConto, D. Pollard, R. B. Alley, I. Velicogna, E. Gasson, N. Gomez, S. Sadai, A. Condron, D. M. Gilford, E. L. Ashe, R. E. Kopp, D. Li, A. Dutton, The Paris climate agreement and future sea-level rise from Antarctica. *Nature* **593**, 83–89 (2021).
7. T. L. Edwards, S. Nowicki, B. Marzeion, R. Hock, H. Goelzer, H. Seroussi, N. C. Jourdain, D. A. Slater, F. E. Turner, C. J. Smith, C. M. McKenna, E. Simon, A. Abe-Ouchi, J. M. Gregory, E. Larour, W. H. Lipscomb, A. J. Payne, A. Shepherd, C. Agosta, P. Alexander, T. Albrecht, B. Anderson, X. Asay-Davis, A. Aschwanden, A. Barthel, A. Bliss, R. Calov, C. Chambers, N. Champollion, Y. Choi, R. Cullather, J. Cuzzone, C. Dumas, D. Felikson, X. Fettweis, K. Fujita, B. K. Galton-Fenzi, R. Gladstone, N. R. Golledge, R. Greve, T. Hattermann, M. J. Hoffman, A. Humbert, M. Huss, P. Huybrechts, W. Immerzeel, T. Kleiner, P. Kraaijenbrink, S. Le clec'h, V. Lee, G. R. Leguy, C. M. Little, D. P. Lowry, J.-H. Malles, D. F. Martin, F. Maussion, M. Morlighem, J. F. O'Neill, I. Nias, F. Pattyn, T. Pelle, S. F. Price, A. Quiquet, V. Radić, R. Reese, D. R. Rounce, M. Rückamp, A. Sakai, C. Shafer, N.-J. Schlegel, S. Shannon, R. S. Smith, F. Straneo, S. Sun, L. Tarasov, L. D. Trusel, J. Van Breedam, R. van de Wal, M. van den Broeke, R. Winkelmann, H. Zekollari, C. Zhao, T. Zhang, T. Zwinger, Projected land ice contributions to twenty-first-century sea level rise. *Nature* **593**, 74–82 (2021).
8. D. Pollard, R. M. DeConto, R. B. Alley, Potential Antarctic ice sheet retreat driven by hydrofracturing and ice cliff failure. *Earth Planet. Sci. Lett.* **412**, 112–121 (2015).
9. J. Garbe, T. Albrecht, A. Levermann, J. F. Donges, R. Winkelmann, The hysteresis of the Antarctic ice sheet. *Nature* **585**, 538–544 (2020).
10. J. Hinkel, J. A. Church, J. M. Gregory, E. Lambert, G. Le Cozannet, J. Lowe, K. L. McInnes, R. J. Nicholls, T. D. Pol, R. Wal, Meeting user needs for sea level rise information: A decision analysis perspective. *Earth's Future* **7**, 320–337 (2019).
11. A. Dutton, A. E. Carlson, A. J. Long, G. A. Milne, P. U. Clark, R. DeConto, B. P. Horton, S. Rahmstorf, M. E. Raymo, Sea-level rise due to polar ice-sheet mass loss during past warm periods. *Science* **349**, aaa4019 (2015).
12. E. Capron, A. Govin, E. J. Stone, V. Masson-Delmotte, S. Mulitza, B. Otto-Bliesner, T. L. Rasmussen, L. C. Sime, C. Waelbroeck, E. W. Wolff, Temporal and spatial structure of multi-millennial temperature changes at high latitudes during the Last Interglacial. *Quat. Sci. Rev.* **103**, 116–133 (2014).
13. M.-V. Guarino, L. C. Sime, D. Schröeder, I. Malmierca-Vallet, E. Rosenblum, M. Ringer, J. Ridley, D. Feltham, C. Bitz, E. J. Steig, E. Wolff, J. Stroeve, A. Sellar, Sea-ice-free Arctic during the Last Interglacial supports fast future loss. *Nat. Clim. Change* **10**, 928–932 (2020).

14. T. L. Edwards, M. A. Brandon, G. Durand, N. R. Edwards, N. R. Golledge, P. B. Holden, I. J. Nias, A. J. Payne, C. Ritz, A. Wernecke, Revisiting Antarctic ice loss due to marine ice-cliff instability. *Nature* **566**, 58–64 (2019).
15. R. M. DeConto, D. Pollard, Contribution of Antarctica to past and future sea-level rise. *Nature* **531**, 591–597 (2016).
16. R. E. Kopp, F. J. Simons, J. X. Mitrovica, A. C. Maloof, M. Oppenheimer, Probabilistic assessment of sea level during the Last Interglacial stage. *Nature* **462**, 863–867 (2009).
17. B. Dyer, J. Austermann, W. J. D'Andrea, R. C. Creel, M. R. Sandstrom, M. Cashman, A. Rovere, M. E. Raymo, Sea-level trends across the Bahamas constrain peak Last Interglacial ice melt. *Proc. Natl. Acad. Sci. U.S.A.* **118**, e2026839118 (2021).
18. A. Dutton, J. M. Webster, D. Zwartz, K. Lambeck, B. Wohlfarth, Tropical tales of polar ice: Evidence of Last Interglacial polar ice sheet retreat recorded by fossil reefs of the granitic Seychelles islands. *Quat. Sci. Rev.* **107**, 182–196 (2015).
19. M. J. O'Leary, P. J. Hearty, W. G. Thompson, M. E. Raymo, J. X. Mitrovica, J. M. Webster, Ice sheet collapse following a prolonged period of stable sea level during the Last Interglacial. *Nat. Geosci.* **6**, 796–800 (2013).
20. N. L. M. Barlow, E. L. McClymont, P. L. Whitehouse, C. R. Stokes, S. S. R. Jamieson, S. A. Woodroffe, M. J. Bentley, S. L. Callard, C. Ó. Cofaigh, D. J. A. Evans, J. R. Horrocks, J. M. Lloyd, A. J. Long, M. Margold, D. H. Roberts, M. L. Sanchez-Montes, Lack of evidence for a substantial sea-level fluctuation within the Last Interglacial. *Nat. Geosci.* **11**, 627–634 (2018).
21. E. J. Rohling, F. D. Hibbert, K. M. Grant, E. V. Galaasen, N. Irvalı, H. F. Kleiven, G. Marino, U. Ninnemann, A. P. Roberts, Y. Rosenthal, H. Schulz, F. H. Williams, J. Yu, Asynchronous Antarctic and Greenland ice-volume contributions to the Last Interglacial sea-level highstand. *Nat. Commun.* **10**, 5040 (2019).
22. C. Hay, J. X. Mitrovica, N. Gomez, J. R. Creveling, J. Austermann, R. E. Kopp, The sea-level fingerprints of ice-sheet collapse during interglacial periods. *Quat. Sci. Rev.* **87**, 60–69 (2014).
23. D. M. Gilford, E. L. Ashe, R. M. DeConto, R. E. Kopp, D. Pollard, A. Rovere, Could the Last Interglacial constrain projections of future Antarctic ice mass loss and sea-level rise? *J. Geophys. Res. Earth* **125**, e2019JF005418 (2020).
24. A. J. Long, N. L. M. Barlow, F. S. Busschers, K. M. Cohen, W. R. Gehrels, L. M. Wake, Near-field sea-level variability in northwest Europe and ice sheet stability during the Last Interglacial. *Quat. Sci. Rev.* **126**, 26–40 (2015).
25. K. Lambeck, A. Purcell, S. Funder, K. H. KjaeR, E. Larsen, P. E. R. Moller, Constraints on the Late Saalian to early Middle Weichselian ice sheet of Eurasia from field data and rebound modelling. *Boreas* **35**, 539–575 (2006).
26. K. Lambeck, A. Purcell, A. Dutton, The anatomy of interglacial sea levels: The relationship between sea levels and ice volumes during the Last Interglacial. *Earth Planet. Sci. Lett.* **315-316**, 4–11 (2012).
27. J. Austermann, J. X. Mitrovica, P. Huybers, A. Rovere, Detection of a dynamic topography signal in Last Interglacial sea-level records. *Sci. Adv.* **3**, e1700457 (2017).
28. A. R. Simms, J. B. Anderson, R. DeWitt, K. Lambeck, A. Purcell, Quantifying rates of coastal subsidence since the Last Interglacial and the role of sediment loading. *Global Planet. Change* **111**, 296–308 (2013).
29. Y. Zhou, J. McManus, Extensive evidence for a Last Interglacial Laurentide outburst (LILO) event. *Geology* **50**, 934–938 (2022).
30. H. T. de la Beche, *The Geology of Cornwall and Devon and Part of W. Somerset* (Memoirs of the Ordnance Geological Survey, 1839).
31. S. Campbell, C. O. Hunt, J. D. Scourse, D. H. Keen, D. G. Croot, Southwest England, in *A Revised Correlation of Quaternary Deposits in the British Isles* (Geological Society of London, 1999), vol. 23, chap. 6, pp. 66–78.
32. S. Campbell, C. O. Hunt, J. D. Scourse, D. H. Keen, N. Stephens, *Quaternary of South-West England* (Geological Conservation Review Series, Springer, 1998).
33. A. Rovere, M. E. Raymo, M. Vacchi, T. Lorscheid, P. Stocchi, L. Gómez-Pujol, D. L. Harris, E. Casella, M. J. O'Leary, P. J. Hearty, The analysis of Last Interglacial (MIS 5e) relative sea-level indicators: Reconstructing sea-level in a warmer world. *Earth Sci. Rev.* **159**, 404–427 (2016).
34. K. M. Cohen, V. Cartelle, R. Barnett, F. S. Busschers, N. L. M. Barlow, Last Interglacial sea-level data points from Northwest Europe. *Earth Syst. Sci. Data* **14**, 2895–2937 (2022).
35. W. R. Peltier, D. F. Argus, R. Drummond, Space geodesy constrains ice age terminal deglaciation: The global ICE-6G_C (VM5a) model. *J. Geophys. Res. Solid Earth* **120**, 450–487 (2015).
36. F. Colleoni, C. Wekerle, J.-O. Näslund, J. Brandefelt, S. Masina, Constraint on the penultimate glacial maximum Northern Hemisphere ice topography (≈140 kyrs BP). *Quat. Sci. Rev.* **137**, 97–112 (2016).
37. R. A. Kendall, J. X. Mitrovica, G. A. Milne, On post-glacial sea level - II. Numerical formulation and comparative results on spherically symmetric models. *Geophys. J. Int.* **161**, 679–706 (2005).
38. R. Calov, A. Robinson, M. Perrette, A. Ganopolski, Simulating the Greenland ice sheet under present-day and palaeo constraints including a new discharge parameterization. *Cryosphere* **9**, 179–196 (2015).
39. A. M. Yau, M. L. Bender, A. Robinson, E. J. Brook, Reconstructing the Last Interglacial at Summit, Greenland: Insights from GISP2. *Proc. Natl. Acad. Sci. U.S.A.* **113**, 9710–9715 (2016).
40. J. S. Hoffman, P. U. Clark, A. C. Parnell, F. He, Regional and global sea-surface temperatures during the last interglaciation. *Science* **355**, 276–279 (2017).
41. D. Farinotti, M. Huss, J. J. Fürst, J. Landmann, H. Machguth, F. Maussion, A. Pandit, A consensus estimate for the ice thickness distribution of all glaciers on Earth. *Nat. Geosci.* **12**, 168–173 (2019).
42. N. R. Golledge, P. U. Clark, F. He, A. Dutton, C. S. M. Turney, C. J. Fogwill, T. R. Naish, R. H. Levy, R. M. McKay, D. P. Lowry, N. A. N. Bertler, G. B. Dunbar, A. E. Carlson, Retreat of the antarctic ice sheet during the last interglaciation and implications for future change. *Geophys. Res. Lett.* **48**, e2021GL094513 (2021).
43. P. U. Clark, F. He, N. R. Golledge, J. X. Mitrovica, A. Dutton, J. S. Hoffman, S. Dendy, Oceanic forcing of penultimate deglacial and Last Interglacial sea-level rise. *Nature* **577**, 660–664 (2020).
44. S. Sun, F. Pattyn, E. G. Simon, T. Albrecht, S. Cornford, R. Calov, C. Dumas, F. Gillet-Chaulet, H. Goelzer, N. R. Golledge, R. Greve, M. J. Hoffman, A. Humbert, E. Kazmierczak, T. Kleiner, G. R. Leguy, W. H. Lipscomb, D. Martin, M. Morlighem, S. Nowicki, D. Pollard, S. Price, A. Quiquet, H. Seroussi, T. Schlemm, J. Sutter, R. S. W. van de Wal, R. Winkelmann, T. Zhang, Antarctic ice sheet response to sudden and sustained ice-shelf collapse (ABUMIP). *J. Glaciol.* **66**, 891–904 (2020).
45. C. S. M. Turney, C. J. Fogwill, N. R. Golledge, N. P. McKay, E. van Sebille, R. T. Jones, D. Etheridge, M. Rubino, D. P. Thornton, S. M. Davies, C. B. Ramsey, Z. A. Thomas, M. I. Bird, N. C. Munksgaard, M. Kohno, J. Woodward, K. Winter, L. S. Weyrich, C. M. Rootes, H. Millman, P. G. Albert, A. Rivera, T. van Ommen, M. Curran, A. Moy, S. Rahmstorf, K. Kawamura, C. D. Hillenbrand, M. E. Weber, C. J. Manning, J. Young, A. Cooper, Early Last Interglacial ocean warming drove substantial ice mass loss from Antarctica. *Proc. Natl. Acad. Sci. U.S.A.* **117**, 3996–4006 (2020).
46. A. S. Hein, J. Woodward, S. M. Marrero, S. A. Dunning, E. J. Steig, S. P. Freeman, F. M. Stuart, K. Winter, M. J. Westoby, D. E. Sugden, Evidence for the stability of the West Antarctic Ice Sheet divide for 1.4 million years. *Nat. Commun.* **7**, 10325 (2016).
47. L. Pan, E. M. Powell, K. Latychev, J. X. Mitrovica, J. R. Creveling, N. Gomez, M. J. Hoggard, P. U. Clark, Rapid postglacial rebound amplifies global sea level rise following West Antarctic Ice Sheet collapse. *Sci. Adv.* **7**, eabf7787 (2021).
48. E. M. Powell, L. Pan, M. J. Hoggard, K. Latychev, N. Gomez, J. Austermann, J. X. Mitrovica, The impact of 3-D earth structure on far-field sea level following interglacial West Antarctic ice sheet collapse. *Quat. Sci. Rev.* **273**, 107256 (2021).
49. Past Interglacials Working Group of PAGES, Interglacials of the last 800,000 years. *Rev. Geophys.* **54**, 162–219 (2016).
50. J. Peng, X. Wang, G. Adamiec, The build-up of the laboratory-generated dose-response curve and underestimation of equivalent dose for quartz OSL in the high dose region: A critical modelling study. *Quat. Geochronol.* **67**, 101231 (2022).
51. A. Murray, J.-P. Buylaert, M. Henriksen, J.-I. Svendsen, J. Mangerud, Testing the reliability of quartz OSL ages beyond the Eemian. *Radiat. Meas.* **43**, 776–780 (2008).
52. S. M. Pawley, P. Toms, S. J. Armitage, J. Rose, Quartz luminescence dating of Anglian Stage (MIS 12) fluvial sediments: Comparison of SAR age estimates to the terrace chronology of the Middle Thames valley, UK. *Quat. Geochronol.* **5**, 569–582 (2010).
53. A. G. Wintle, A. S. Murray, A review of quartz optically stimulated luminescence characteristics and their relevance in single-aliquot regeneration dating protocols. *Radiat. Meas.* **41**, 369–391 (2006).
54. R. F. Galbraith, R. G. Roberts, G. M. Laslett, H. Yoshida, J. M. Olley, Optical dating of single and multiple grains of quartz from Jinmium Rock Shelter, Northern Australia: Part I, Experimental design and statistical models. *Archaeometry* **41**, 339–364 (1999).
55. K. J. Thomsen, A. S. Murray, M. Jain, L. Bøtter-Jensen, Laboratory fading rates of various luminescence signals from feldspar-rich sediment extracts. *Radiat. Meas.* **43**, 1474–1486 (2008).
56. C. J. Oldknow, A. S. Carr, J. M. Hooke, Z. Shen, The suitability of a low temperature post-IR IRSL signal for dating alluvial and colluvial "cut and fill" sequences in the Great Karoo, South Africa. *Quat. Geochronol.* **58**, 101064 (2020).
57. M. Auclair, M. Lamothe, S. Huot, Measurement of anomalous fading for feldspar IRSL using SAR. *Radiat. Meas.* **37**, 487–492 (2003).
58. J.-P. Buylaert, M. Jain, A. S. Murray, K. J. Thomsen, C. Thiel, R. Sohbati, A robust feldspar luminescence dating method for Middle and Late Pleistocene sediments. *Boreas* **41**, 435–451 (2012).

59. T. Lorscheid, A. Rovere, The indicative meaning calculator—Quantification of paleo sea-level relationships by using global wave and tide datasets. *Open Geospatial Data Softw. Standards* **4**, 10 (2019).
60. I. Shennan, Long, A.J., Horton, B.P., Handbook of sea-level research: Framing research questions, in *Handbook of Sea-Level Research*, I. Shennan, A. J. Long, B. P. Horton, Eds. (Wiley, 2015), pp. 3–28.
61. T. Lorscheid, T. Felis, P. Stocchi, J. C. Obert, D. Scholz, A. Rovere, Tides in the Last Interglacial: Insights from notch geometry and palaeo tidal models in Bonaire, Netherland Antilles. *Sci. Rep.* **7**, 16241 (2017).
62. P. Scussolini, J. Dullaart, S. Muis, A. Rovere, P. Bakker, D. Coumou, H. Renssen, P. J. Ward, J. C. J. H. Aerts, Modeled storm surge changes in a warmer world: The Last Interglacial. *Clim. Past* **19**, 141–157 (2023).
63. O. A. Dumitru, J. Austermann, V. J. Polyak, J. J. Fornos, Y. Asmerom, J. Gines, A. Gines, B. P. Onac, Constraints on global mean sea level during Pliocene warmth. *Nature* **574**, 233–236 (2019).
64. L. E. Lisiecki, M. E. Raymo, A pliocene-pleistocene stack of 57 globally distributed benthic $\delta^{18}O$ records. *Paleoceanography* **20**, PA1003 (2005).
65. K. G. Miller, J. V. Browning, W. J. Schmelz, R. E. Kopp, G. S. Mountain, J. D. Wright, Cenozoic sea-level and cryospheric evolution from deep-sea geochemical and continental margin records. *Sci. Adv.* **6**, eaaz1346 (2020).
66. P. Japsen, T. Bidstrup, E. S. Rasmussen, Comment on: Cenozoic evolution of the eastern Danish North Sea by M. Huuse, H. Lykke-Andersen and O. Michelsen, [Marine Geology 177, 243–269]. *Mar. Geol.* **186**, 571–575 (2002).
67. E. S. Rasmussen, K. Dybkjær, S. Piasecki, Lithostratigraphy of the upper Oligocene–Miocene succession of Denmark. *Geol. Surv. Denmark Greenland Bull.* **22**, 1–92 (2020).
68. T. Eidvin, F. Riis, E. S. Rasmussen, Oligocene to lower pliocene deposits of the Norwegian continental shelf, Norwegian Sea, Svalbard, Denmark and their relation to the uplift of Fennoscandia: A synthesis. *Mar. Pet. Geol.* **56**, 184–221 (2014).
69. E. S. Rasmussen, Stratigraphy and depositional evolution of the uppermost Oligocene –Miocene succession in western Denmark. *Bull. Geol. Soc. Denmark* **51**, 89–109 (2004).
70. A. M. Dziewonski, D. L. Anderson, Preliminary reference Earth model. *Phys. Earth Planet. In.* **25**, 297–356 (1981).
71. C. Waelbroeck, L. Labeyrie, E. Michel, J. C. Duplessy, J. F. McManus, K. Lambeck, E. Balbon, M. Labracherie, Sea-level and deep water temperature changes derived from benthic foraminifera isotopic records. *Quat. Sci. Rev.* **21**, 295–305 (2002).
72. C. L. Batchelor, M. Margold, M. Krapp, D. K. Murton, A. S. Dalton, P. L. Gibbard, C. R. Stokes, J. B. Murton, A. Manica, The configuration of Northern Hemisphere ice sheets through the Quaternary. *Nat. Commun.* **10**, 3713 (2019).
73. S. Dendy, J. Austermann, J. R. Creveling, J. X. Mitrovica, Sensitivity of Last Interglacial sea-level high stands to ice sheet configuration during marine isotope stage 6. *Quat. Sci. Rev.* **171**, 234–244 (2017).
74. E. J. Rohling, F. D. Hibbert, F. H. Williams, K. M. Grant, G. Marino, G. L. Foster, R. Hennekam, G. J. de Lange, A. P. Roberts, J. Yu, J. M. Webster, Y. Yokoyama, Differences between the last two glacial maxima and implications for ice-sheet, $\delta^{18}O$, and sea-level reconstructions. *Quat. Sci. Rev.* **176**, 1–28 (2017).
75. J. D. Shakun, D. W. Lea, L. E. Lisiecki, M. E. Raymo, An 800-kyr record of global surface ocean $\delta^{18}O$ and implications for ice volume-temperature coupling. *Earth Planet. Sci. Lett.* **426**, 58–68 (2015).
76. L. Tarasov, A. Hughes, R. Gyllencreutz, O. S. Lohne, J. Mangerud, J. I. Svendsen, paper presented at the IGS Symposium on Contribution of Glaciers and Ice Sheets to Sea-Level Change (2014).
77. A. L. Thomas, G. M. Henderson, P. Deschamps, Y. Yokoyama, A. J. Mason, E. Bard, B. Hamelin, N. Durand, G. Camoin, Penultimate deglacial sea-level timing from uranium/thorium dating of Tahitian corals. *Science* **324**, 1186–1189 (2009).
78. A. Quiquet, C. Ritz, H. J. Punge, D.Salas y Mélia, Greenland ice sheet contribution to sea level rise during the Last Interglacial period: A modelling study driven and constrained by ice core data. *Clim. Past* **9**, 353–366 (2013).
79. H. Goelzer, P. Huybrechts, M.-F. Loutre, T. Fichefet, Last Interglacial climate and sea-level evolution from a coupled ice sheet–climate model. *Clim. Past* **12**, 2195–2213 (2016).
80. S. L. Bradley, T. J. Reerink, R. S. W. van de Wal, M. M. Helsen, Simulation of the Greenland Ice Sheet over two glacial–Interglacial cycles: Investigating a sub-ice- shelf melt parameterization and relative sea level forcing in an ice-sheet–ice-shelf model. *Clim. Past* **14**, 619–635 (2018).
81. J. D. Scourse, Late pleistocene stratigraphy of North and West Cornwall. *Trans. R. Geol. Soc. Cornwall* **22**, 2–56 (1996).
82. H. L. James, Raised beaches of West Cornwall and their evolving chronology. *Proc. Ussher Soc.* **8**, 437–440 (1995).
83. H. C. L. James, Aspects of the raised beaches of South Cornwall. *Proc. Ussher Soc.* **2**, 55–56 (1968).
84. H. C. L. James, Pleistocene sections as Gerrans Bay, south Cornwall. *Proc. Ussher Soc.* **5**, 238 (1981).
85. G. A. T. Duller, *Luminescence Dating: Guidelines on Using Luminescence Dating in Archaeology* (English Heritage, 2008).
86. G. Masselink, T. Scott, T. Poate, P. Russell, M. Davidson, D. Conley, The extreme 2013/2014 winter storms: Hydrodynamic forcing and coastal response along the southwest coast of England. *Earth Surf. Process. Landf.* **41**, 378–391 (2015).
87. M. T. Leveridge, A. J. J. Goode, R. C. Scrivener, R. A. Monkhouse, British Geological Survey, *Geology of the Country Around Falmouth: Memoir for the 1:50 000 Geological Sheet 352 (England & Wales)* (Memoirs of the Geological Survey of Great Britain, England and Wales (Sheet - New Series), HMSO, 1990).
88. H. C. L. James, The coastal palaeo-morphology of West Cornwall with particular reference to shore (wave-cut) platforms. *Trans. R. Geol. Soc. Cornwall* **22**, 121–144 (2003).
89. M. D. Bateman, J. A. Catt, An absolute chronology for the raised beach and associated deposits at Sewerby, East Yorkshire, England. *J. Quat. Sci.* **11**, 389–395 (1996).
90. A. G. Wintle, Luminescence dating: Laboratory procedures and protocols. *Radiat. Meas.* **27**, 769–817 (1997).
91. M. J. Aitken, *Thermoluminescence Dating* (Academic Press, 1985).
92. M. J. Aitken, *An Introduction to Optical Dating. The Dating of Quaternary Sediments by the Use of Photon-Stimulated Luminescence* (Oxford Univ. Press, 1998).
93. G. Guerin, N. Mercier, G. Adamiec, Dose-rate conversion factors: Update. *Ancient TL* **29**, 5–8 (2011).
94. S. Balescu, M. Lamothe, Thermoluminescence dating of the holsteinian marine formation of Herzeele, northern France. *J. Quat. Sci.* **8**, 117–124 (1993).
95. D. J. Huntley, D. J. Baril, The K content of the K-feldspars being measured in optical dating or in thermoluminescence dating. *Ancient TL* **15**, 11–13 (1997).
96. D. J. Huntley, R. G. V. Hancock, The Rb contents of the K-feldspars being measured in optical dating. *Ancient TL* **19**, 43–46 (2001).
97. J. R. Prescott, J. T. Hutton, Cosmic ray contributions to dose rates for luminescence and ESR dating: Large depths and long-term time variations. *Radiat. Meas.* **23**, 497–500 (1994).
98. A. S. Murray, A. G. Wintle, Luminescence dating of quartz using an improved single-aliquot regenerative-dose protocol. *Radiat. Meas.* **32**, 57–73 (2000).
99. A. S. Murray, A. G. Wintle, The single aliquot regenerative dose protocol: Potential for improvements in reliability. *Radiat. Meas.* **37**, 377–381 (2003).
100. G. A. T. Duller, Assessing the error on equivalent dose estimates derived from single aliquot regenerative dose measurements. *Ancient TL* **25**, 15–24 (2007).
101. A. C. Cunningham, J. Wallinga, Selection of integration time intervals for quartz OSL decay curves. *Quat. Geochronol.* **5**, 657–666 (2010).
102. S. J. Armitage, R. M. Bailey, The measured dependence of laboratory beta dose rates on sample grain size. *Radiat. Meas.* **39**, 123–127 (2005).
103. J. P. Buylaert, A. S. Murray, K. J. Thomsen, M. Jain, Testing the potential of an elevated temperature IRSL signal from K-feldspar. *Radiat. Meas.* **44**, 560–565 (2009).
104. A. G. Wintle, Anomalous fading of thermo-luminescence in mineral samples. *Nature* **245**, 143–144 (1973).
105. D. J. Huntley, M. Lamothe, Ubiquity of anomalous fading in K-feldspars and the measurement and correction for it in optical dating. *Can. J. Earth Sci.* **38**, 1093–1106 (2001).
106. M. Jain, J. P. Buylaert, K. J. Thomsen, A. S. Murray, Further investigations on 'non-fading' in K-feldspar. *Quat. Int.* **362**, 3–7 (2015).
107. J. Wallinga, A. Murray, A. Wintle, The single-aliquot regenerative-dose (SAR) protocol applied to coarse-grain feldspar. *Radiat. Meas.* **32**, 529–533 (2000).
108. R. Westaway, Cenozoic uplift of southwest England. *J. Quat. Sci.* **25**, 419–432 (2010).
109. J. R. Lee, I. Candy, R. Haslam, The neogene and quaternary of England: Landscape evolution, tectonics, climate change and their expression in the geological record. *Proc. Geol. Assoc.* **129**, 452–481 (2018).
110. K. Pedoja, J. Jara-Muñoz, G. De Gelder, J. Robertson, M. Meschis, D. Fernandez-Blanco, M. Nexer, Y. Poprawski, O. Dugué, B. Delcaillau, P. Bessin, M. Benabdelouahed, C. Authemayou, L. Husson, V. Regard, D. Menier, B. Pinel, Neogene-Quaternary slow coastal uplift of Western Europe through the perspective of sequences of strandlines from the Cotentin Peninsula (Normandy, France). *Geomorphology* **303**, 338–356 (2018).
111. J.-P. Lautridou, S. Baize, M. Clet, J.-P. Coutard, J.-C. Ozouf, Les séquences plio-pléistocènes littorales et estuariennes de Normandie [Littoral and estuarine Plio-Pleistocene sequences in Normandy (France)]. *Quaternaire* **10**, 161–169 (1999).
112. O. Dugué, The Pliocene to Early Pleistocene marine to fluviatile succession of the Seuil du Cotentin basins (Armorican Massif, Normandy, France). *J. Quat. Sci.* **18**, 215–226 (2003).
113. J. Robson, The recent geology of Cornwall. *Trans. R. Geol. Soc. Cornwall* **17**, 132–163 (1944).
114. D. Brunsden, The erosion surfaces of the river dart. *Proc. Ussher Soc.*, 35–36 (1962).

115. B. Coque-Delhuille, "Le massif du Sud-ouest Anglais et sa bordure sédimentaire; étude géomorphologique," thesis, Université de Paris Panthenon Sorbonne (1987).
116. H. B. Milner, The nature and origin of the pliocene deposits of the county of Cornwall, and their bearing on the pliocene geography of the south-west of England. *Quart. J. Geol. Soc.* **78**, 348–377 (1922).
117. A. A. Miller, The 600-foot plateau in Pembrokeshire and Carmarthenshire. *Geogr. J.* **90**, 148–159 (1937).
118. W. G. V. Balchin, The erosion surfaces of exmoor and adjacent areas. *Geogr. J.* **118**, 453 (1952).
119. A. C. Bishop, in *Classic Areas of British Geology, London* (British Geological Service, 1989).
120. D. H. Keen, Pre-Flandrian Quaternary deposits, landforms and environments, in *The Quaternary of Jersey. Quaternary Research Association Field Guide*, Quaternary Research Association, D. H. Keen, Ed. (1993).
121. J. F. N. Green, The terraces of Bournemouth, Hants. *Proc. Geol. Assoc.* **57**, 82–101 (1946).
122. C. E. Everard, Erosion platforms on the borders of the Hampshire Basin. *Trans. Inst. Br. Geogr.* **22**, 33–46 (1956).
123. R. Westaway, D. Bridgland, M. White, The Quaternary uplift history of central southern England: Evidence from the terraces of the Solent River system and nearby raised beaches. *Quat. Sci. Rev.* **25**, 2212–2250 (2006).

Acknowledgments: We acknowledge PALSEA, a working group of the International Union for Quaternary Sciences (INQUA) and Past Global Changes (PAGES), which in turn received support from the Swiss Academy of Sciences and the Chinese Academy of Sciences. Special thanks go to D. Charman (University of Exeter) for commenting on an early draft of the manuscript and for career mentorship to R.L.B. **Funding:** R.L.B. acknowledges a Research Fellowship from the University of Exeter and funding from the Sécurité publique du Québec to the University of Quebec at Rimouski. J.A., B.D., and R.C.C. acknowledge funding from NSF grant OCE-1841888. J.A. acknowledges support from the Vetlesen Foundation. N.L.M.B. received support for this work from European Research Council (ERC) under the European Union's Horizon 2020 research and innovation programme (RISeR, grant agreement no. 802281). M.W.T. and S.J.B. received funding for fieldwork from the University of Plymouth's Marine Institute. J.A. acknowledges computing resources from Columbia University's Shared Research Computing Facility project, which is supported by NIH Research Facility Improvement Grant 1G20RR030893-01, and associated funds from the New York State Empire State Development, Division of Science Technology and Innovation (NYSTAR) contract C090171, both awarded 15 April 2010. **Author contributions:** Conceptualization: R.L.B., J.A., B.D., M.W.T., R.C.C., and N.L.M.B. Methodology: R.L.B., J.A., B.D., and R.C.C. Software: J.A. and B.D. Validation: J.A. and B.D. Formal analysis: J.A., B.D., and M.W.T. Investigation: A.S.C., S.J.B., M.W.T., and R.C.C. Resources: A.S.C. Data curation: R.L.B. Visualization: R.L.B., J.A., B.D., and R.C.C. Supervision: N.L.M.B. Writing—original draft: R.L.B., J.A., and B.D. Writing—review and editing: R.L.B., J.A., B.D., A.S.C., S.J.B., M.W.T., R.C.C., and N.L.M.B. Funding acquisition: M.W.T., S.J.B., N.L.M.B., and J.A. **Competing interests:** The authors declare that they have no competing interests. **Data and materials availability:** Relevant code, model input, and output is available on Zenodo (https://doi.org/10.5281/zenodo.7955458). While the code is contained in the Zenodo repository, the Bayesian inversion code (https://github.com/blakedyer/bahamas_lig/tree/europe_lig) and the GIA code (https://github.com/jaustermann/SLcode/) are also available on GitHub. All sea-level and OSL data are available in the main text or the supplementary excel sheet. All data needed to evaluate the conclusions in the paper are present in the paper and/or the Supplementary Materials.

Submitted 23 September 2022
Accepted 5 June 2023
Published 5 July 2023
10.1126/sciadv.adf0198